



Research article

Ni doping induced property enhancement in laser ablated BaSnO₃ films suitable for optoelectronic applications

Jibi John^a, S. Suresh^{a,b}, M. Sivakumar^c, K.G. Gopchandran^a, V.P. Mahadevan Pillai^{a,c,*}^a Department of Optoelectronics, University of Kerala, Thiruvananthapuram, Kerala, India^b Department of Electronics, SreeAyyappa College, Chengannur, Kerala, India^c Department of Physics, Amrita School of Physical Sciences, Coimbatore, Amrita Vishwa Vidyapeetham, India

ARTICLE INFO

Keywords:

Perovskite oxide
BaSnO₃ films
Pulsed laser deposition
Refractive index
Induced magnetic field-assisted particle convergence effect
Bandgap renormalization

ABSTRACT

Pulsed laser deposition is a straightforward approach for preparing films with superconducting to dielectric properties with atomic layer precision. The deep-seated mechanisms involved in the particle transport from target to substrate and subsequent film formation still need to be fully comprehended. This manuscript reports the property enhancement observed in laser ablated perovskite BaSnO₃ films with Ni doping. Films' crystallinity improvement is observed, and an intensity enhancement of 1150% is observed on 3 mol% Ni-doping. The optimum Ni-doping concentration in BaSnO₃ is found to be 3 mol%. Herein, Ni-doped BaSnO₃ films deposited by PLD showed an unusual increase in film thickness (i.e., from 615 nm in the pure film to 1317 nm in the film with 7 mol% Ni-doping as revealed by lateral SEM analysis and spectroscopic ellipsometry). We propose an "Induced Magnetic field-assisted Particle Convergence (IMPC)" effect for this superficial growth enhancement. The film's optical properties are modified with an increased nickel doping level, and the bandgap energy shows renormalization. All the films show excellent transmittance (80–90%) in the Vis.-NIR region. Hall-effect measurement reveals the increased carrier concentration by three orders (2.98×10^{11} to 3.50×10^{14} cm⁻³). In addition, the enhancement in mobility from 3.13 to 20.93 cm²V⁻¹s⁻¹ and a decrease in electrical resistivity by six orders (i.e., from 4.05×10^9 to 1.13×10^3 Ω cm) are observed on 7 mol% Ni doping. XPS measurements reveals that the Ba, Sn and Ni ions are at 2+, 4+ and 2+ oxidation states. Using spectroscopic ellipsometric method, we estimated the optical constants of the films, the refractive index, dielectric constant, and extinction coefficient show a normal dispersion behavior. The high crystallinity, high transmittance, suitable surface topography, and improved electrical performances of the Ni-doped BaSnO₃ films make them excellent candidates for optoelectronic devices and solar cells.

1. Introduction

BaSnO₃, having an ABO₃ structure where Ca, Sr, or Ba at site A and a transition metal at site B, belongs to the perovskite oxide family [1]. Perovskite oxide films are gaining much attention as a TCO because of their physical properties [1–3]. BaSnO₃ is a (n-type)

* Corresponding author. Department of Optoelectronics, University of Kerala, Thiruvananthapuram, Kerala, India.
E-mail addresses: vpmpillai9@gmail.com, mahadevanpillai@amrita.edu (V.P.M. Pillai).

<https://doi.org/10.1016/j.heliyon.2024.e26688>

Received 21 December 2023; Accepted 18 February 2024

Available online 20 February 2024

2405-8440/© 2024 The Authors. Published by Elsevier Ltd. This is an open access article under the CC BY-NC license (<http://creativecommons.org/licenses/by-nc/4.0/>).

wide bandgap semiconductor ($E_g = 3.1$ eV) with a cubic perovskite structure [4,5]. Various ways to prepare BaSnO_3 have been reported [6,7]. With the proper substitution at Ba and Sn cation sites, the film properties of BaSnO_3 can be modified [8]. The pure and doped forms of BaSnO_3 find an essential application in thermally stable and ceramic boundary layer capacitors [9]. It can be used as a sensor material for gases such as CO, NO, and Cl and humidity sensors [6–10]. The properties of perovskite oxides get altered or modulated by doping, and new exciting features are obtained by elemental substitution of transition elements.

Upadhyay et al. reported nickel doping in BaSnO_3 by the self-combustion method and investigated it for humidity-sensing application [10]. In BaSnO_3 , nickel can be substituted in both Ba and Sn sites. Upendra Kumar et al. reported that nickel-doped BaSnO_3 is useful in spintronic device applications [11]. Kumar et al. observed decreased crystallite size and lattice strain in Ni-doped BaTiO_3 films without undergoing any crystal structure phase change [12]. $\text{BaSn}_{(1-x)}\text{Y}_x\text{O}_{3-\delta}$ compounds showed a p-type and ionic behavior in an oxidative and slightly reducing ambience [13]. Y-doped BaSnO_3 with ZnO additive shows a perovskite cubic single phase and can have potential applications for fuel cell technologies [14]. Liu et al., while doping Sb in BaSnO_3 , observed a reduced optical transmittance and a subsequent widening of bandgap energy in BaSnO_3 . These films exhibit a resistivity of 2.43 m Ω cm, mobility of 1.75 cm²V⁻¹s⁻¹, and carrier concentration of 1.65×10^{21} cm⁻³ [15]. Anoop et al. deposited La-doped BaSnO_3 epitaxial films (substrate- SrTiO_3) by PLD and observed that Sn^{2+} defects produced on vacuum-annealing can control their electrical properties [16]. Laser-ablated Fe-doped BaSnO_3 films on SrTiO_3 substrates under an oxygen partial pressure of 300 mTorr show a highly crystalline nature [17]. Shahid et al. reported the crystal structure of sol-gel prepared Ni-doped BaSrTiO_3 films [18]. Singh et al. observed a strong volumetric strain dependence on the bandgap and the index of refraction in BaSnO_3 films [19]. Sumitra et al. [20] investigated the optical bandgap tuning of Co-doped BaSnO_3 nanostructures. Sharma et al. [21] found that Ni-doped (5 wt%) BiFeO_3 film increases bandgap energy from 2.85 to 3.18 eV. Gao et al. [22] fabricated Co: BaSnO_3 films (substrate- MgO) by PLD and observed that the bandgap energy increases first and then decreases with doping concentration increases. Zhang et al. [23] deposited Cr-doped BaSnO_3 films (substrate- F-doped SnO_2) with the colloidal solution approach. They found that the deposited nanoporous perovskite structures have tunable bandgap energy and have various applications in photoelectric devices. Our previous investigations reported the nonlinear optical and magnetic properties of Ni-doped, Mn-doped, and Fe-doped BaSnO_3 powder samples [24–26]. Further, the supercapacitor behavior of Mn-doped BaSnO_3 powders is also reported [25]. We expect the modified optical and electrical properties of BaSnO_3 by Ni-doping. Ni^{2+} ions when substituted for Sn^{4+} ions in the host lattice we can expect an enhancement in the properties of doped BaSnO_3 . Also, Ni can introduce shallow energy levels in the forbidden energy gap region, which can modify the material's bandgap. Considering these aspects, we have selected Ni as a dopant for the present study.

Because of its versatile and flexible physical vapor phase, Pulsed Laser Deposition (PLD) is one of the best techniques to obtain high-quality pure and doped BaSnO_3 films. This manuscript reports the deposition of pure and Ni-doped BaSnO_3 films (substrate-quartz) by

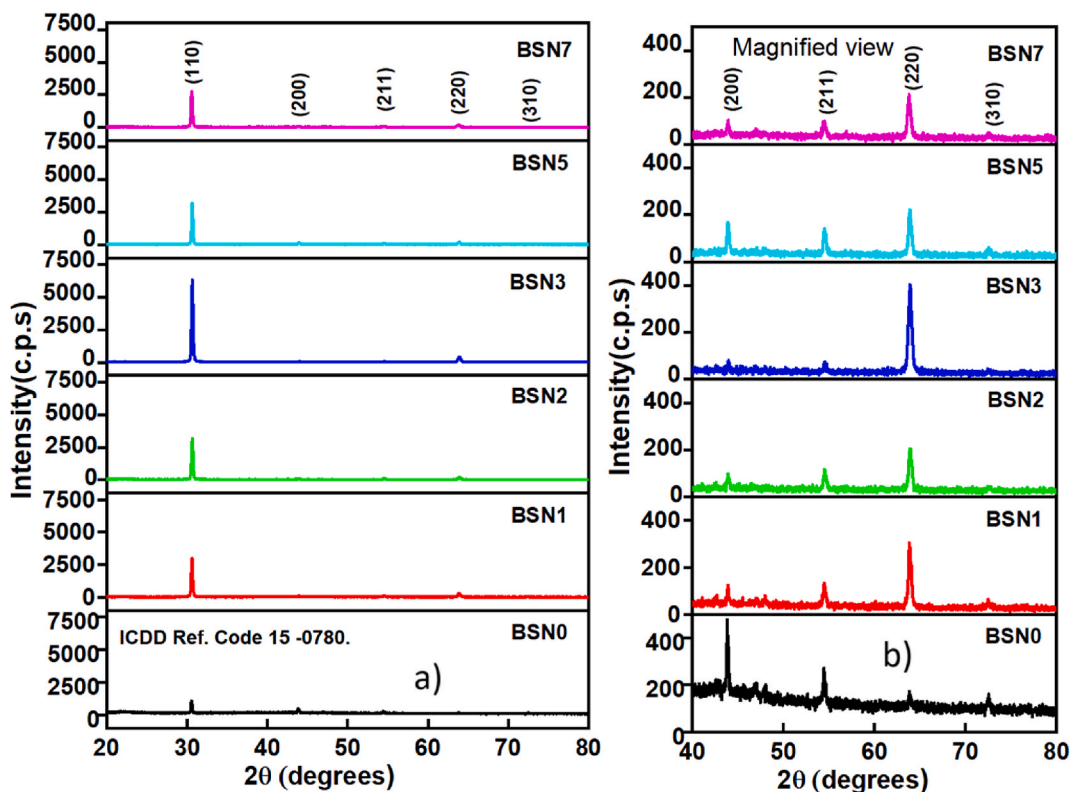


Fig. 1. a) XRD patterns of BaSnO_3 films with different Ni doping levels, and b) magnified view of the selected region to display less intense peaks.

PLD and the investigation of the impact of Ni-doping on their various properties.

2. Materials and methods

The BaSnO₃ and Ni-doped BaSnO₃ powders were prepared using a solid-state ceramic approach. We prepare the pellets by mixing the high-purity BaCO₃, SnO₂, and NiO powders with acetone for 6 h and heating at 1250 °C for 6 h. The prepared pellets were sintered at 1000 °C for 6 h and used as the target material. The pure and Ni-doped BaSnO₃ films are laser deposited as explained in our earlier studies [27,28] with the following deposition parameters viz. substrate-quartz, duration- 45 min, laser energy - 60 mJ, oxygen pressure - 0.02 mbar, the temperature on the substrate - 600 °C, annealing - 900 °C). The BaSnO₃ films with 0, 1, 2, 3, 5, and 7 mol% Ni doping are termed BSN0, BSN1, BSN2, BSN3, BSN5, and BSN7 respectively. The Ni-doped BaSnO₃ films were investigated for their structural, optical, morphological, and electrical properties in detail (see the supplementary Information for description).

3. Results and analysis

XRD data (Fig. 1) of BaSnO₃ films doped with different nickel concentrations ($x = 0, 1, 2, 3, 5,$ and 7 mol%) show the polycrystalline nature with cubic phase (ICDD Ref. Code 15–0780) [12,23]. The BSN0 film shows two strong peaks for 2θ values at 30.61° and 43.98° and three less intense peaks at $54.72, 63.84,$ and 72.64° and they correspond respectively to (110), (200), (211), (220) and (310) planes of BaSnO₃ cubic phase. The highest intensity of the (110) peak suggests that (110) is the preferred growth orientation in the BSN0 film. The (110) peak intensity increases with the enhancement in Ni doping level up to 3 mol% and shows a slight decrease afterward. In all the Ni-doped films, $\langle 110 \rangle$ remains the preferred crystal growth direction. The (110) peak intensity for the films with Ni doping, viz., 1, 2, 3, 5, & 7 mol %, are respectively 5.5, 5.8, 11.5, 6, and 5.1 times that of BSN0. This enormous increase in intensity with Ni doping suggests the improvement of crystallinity with Ni doping and indicates that the dopant Ni atoms act as new centers of crystal growth. For the BSN0, the I_{200}/I_{220} intensity ratio is 0.217. Ni doping, shows a shift in the intensity from the (200) to (220) peak. The relative (220) peak intensity to that of (200) in the films with 1, 2, 3, 5, & 7 mol %, Ni doping levels are respectively 2.00, 2.61, 8.58, 5.53, and 5.5 [Fig. S 1(a), supplementary Information], and this suggests the promotion of crystal growth along $\langle 110 \rangle$ direction by the dopant Ni atom.

The Ni-doped films show no additional peaks other than BaSnO₃ in the XRD pattern. The BSN0 film shows a FWHM (β_{110}) of 0.22° for the (110) peak. The Ni-doped films show less β_{110} value as compared to that of BSN0 film. The reduction in β_{110} value with Ni doping also suggests the improvement of crystallinity. The $\beta_{(110)}$ also shows an initial decrease with Ni doping up to 3 mol% and increases then [Fig. S1(b), supplementary information]. The maximum intensity and the lowest FWHM value of the most preferred orientation (110) plane for the BSN3 film indicate its highest crystalline quality. The defects and disorders introduced in the films on heavy doping can be the reason for the slight reduction in crystallinity observed in the films with higher doping levels. Thus, 3 mol % is the optimum doping level for Ni in BaSnO₃ film. The improvement in crystallinity observed in the Ni-doped films can also attributed to the enhanced value of thickness (as revealed by the vertical SEM analysis and spectroscopic ellipsometric analysis). The heavy-doped films show higher thickness values than that for low or moderate doping. However, the films with rich doping exhibit a slight reduction in crystalline quality compared to that of the BSN3 film. The tendency to reduce crystallinity due to the formation of defects and disorder on heavy doping nullifies the propensity to improve crystallinity due to the enhancement in thickness in highly Ni-doped films.

The position of the most intense (110) peak shifts systematically towards a higher 2θ value, with Ni doping concentration enhanced [Fig. S1(c), supplementary Information]. The ionic radii of Ni²⁺ is 0.63 Å, and that of Ni³⁺ is 0.56 Å, and are lesser than the ionic radius of Sn⁴⁺ = 0.69 Å [12,29]. Thus, Ni can easily occupy the site of Sn. Since the ionic radii of Ni ions are less than that of the Sn⁴⁺ ions, the substitution of Ni ions in the Sn⁴⁺ site results in the contraction of the lattice and can lead to tensile stress in the films. The observed shift of 110 peak towards the higher 2θ range with Ni doping can be due to Ni substitution. The observed systematic reduction in lattice

Table 1
Structural parameters of BaSnO₃ films.

Sample code	$\beta_{(110)}$ (°)	Crystallite size (nm)		Lattice strain	Lattice constant (nm)	RMS surface roughness (nm)	Thickness (nm)	
		Scherer Equation	WH plot				FESEM	Ellipsometric analysis
BSN0	0.220	35	56 ± 15	0.0027 ± 0.0007	4.126	4.21	615	606.12 ± 0.7
BSN1	0.219	36	62 ± 13	0.0036 ± 0.0014	4.125	10.94	712	704.15 ± 0.26
BSN2	0.210	38	74 ± 16	0.0048 ± 0.0006	4.120	10.38	771	760.23 ± 0.46
BSN3	0.209	39	85 ± 10	0.0048 ± 0.0018	4.118	2.33	1240	1210 ± 0.49
BSN5	0.211	37	76 ± 7	0.0076 ± 0.0001	4.117	3.77	1306	1291 ± 0.78
BSN7	0.218	36	79 ± 11	0.0055 ± 0.0005	4.116	8.32	1317	1303 ± 1.3

constant with Ni doping enhancement [Fig. S1(d), supplementary information, and Table 1] indicate lattice contraction due to Ni doping.

We used the Scherrer formula to calculate the crystallite size (Table 1) [30]. The crystallite size of the films is also estimated (Table 1) using the Williamson–Hall (W–H) relation [Fig. S2 supplementary information] [30], which is higher than that obtained from Scherer formulae, indicating the broadening of peaks due to strain. The strain value for BSN0 is less than those estimated for doped films.

FESEM images (Fig. 2) give the surface topography of the BaSnO₃ films. The growth mechanism exhibited by BaSnO₃ film is the Stranski–Krastnov intermediate growth [27]. Initially, a layer-by-layer (Frank–Van der Merwe) deposition occurs. The growth mechanism changes to the Volmer–Weber 3D island growth due to the enhanced elastic strain energy when the film thickness is large [28]. The FESEM image of BSN0 presents a continuous film with regular distinct islands, which confirms the Stranski–Krastnov intermediate growth mechanism. The surface morphology of BSN1 shows a similar pattern but with a more significant number of such discrete islands, and this number increases with nickel doping concentration enhancement up to 3 mol%. The BSN3 film shows a dense distribution of such distinct islands with clear grain boundaries. The microstructure of BSN3 presents grains of larger size which are in highly ordered orientation and this can be one of the reason for its superior crystalline quality. The FESEM image of BSN7 presents a

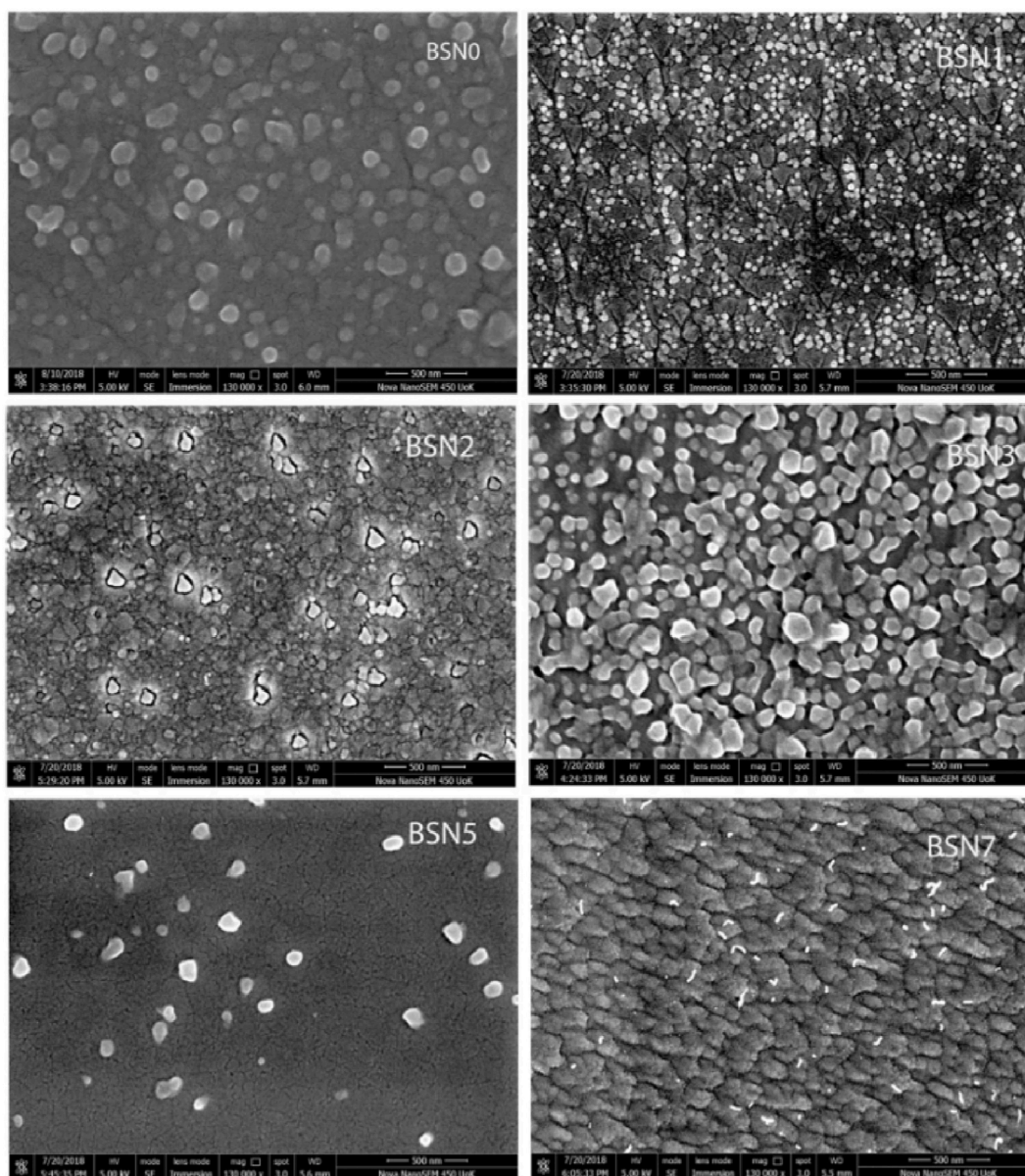


Fig. 2. FESEM images of Ni doped BaSnO₃ films.

dense distribution of well-aligned separate islands with clear grain boundaries. The microstructure of all films have a smooth pinhole free surface suitable for optoelectronic applications.

The EDS spectra confirms nickel presence in BaSnO₃ films (Fig. 3). The elemental composition estimated from EDX analysis is shown in Fig. 3(e). The Ni concentration calculated from the films are slightly lesser than that in the PLD target. But it shows a linear relationship with that in the PLD target (Fig. 3(f)).

Fig. 4 presents the lateral SEM micrographs of BaSnO₃ films, and we estimated the film thickness from them. We observed that the film thickness enhanced regularly with a dopant level increase. Table 1 gives the estimated film thickness of BaSnO₃ films, and the thickness variation with Ni doping is plotted (Fig. 5). Interestingly, a remarkable hike in thickness from ~615 nm in BSN0 film to ~1317 nm in BSN7 film was observed. Hence, we also carried out the film thickness estimation using the ellipsometric measurements with a three-layer model and the fitment of data acquired with a low χ^2 value. The ellipsometric analysis also presents a similar trend in thickness variation (606.12 ± 0.7 nm for BSN0 and 1303 ± 1.3 nm for BSN7) (Table 1 and Fig. 5). The only other factor that can stimulate the film growth is the presence of Ni in the plasma generated and subsequent plasma expansion and transport.

In the PLD method, the laser radiation is focused on the target surface. The laser light ablates the target material and creates a plasma plume. The huge temperature difference between the point of plasma generation and the surroundings paves the way for an adiabatic expansion of the plume. This adiabatic expansion guides the particles to move in a direction perpendicular to the target surface. Thin film condensed on a substrate from the ablated species placed at an angle opposite to the target. A stoichiometric transfer

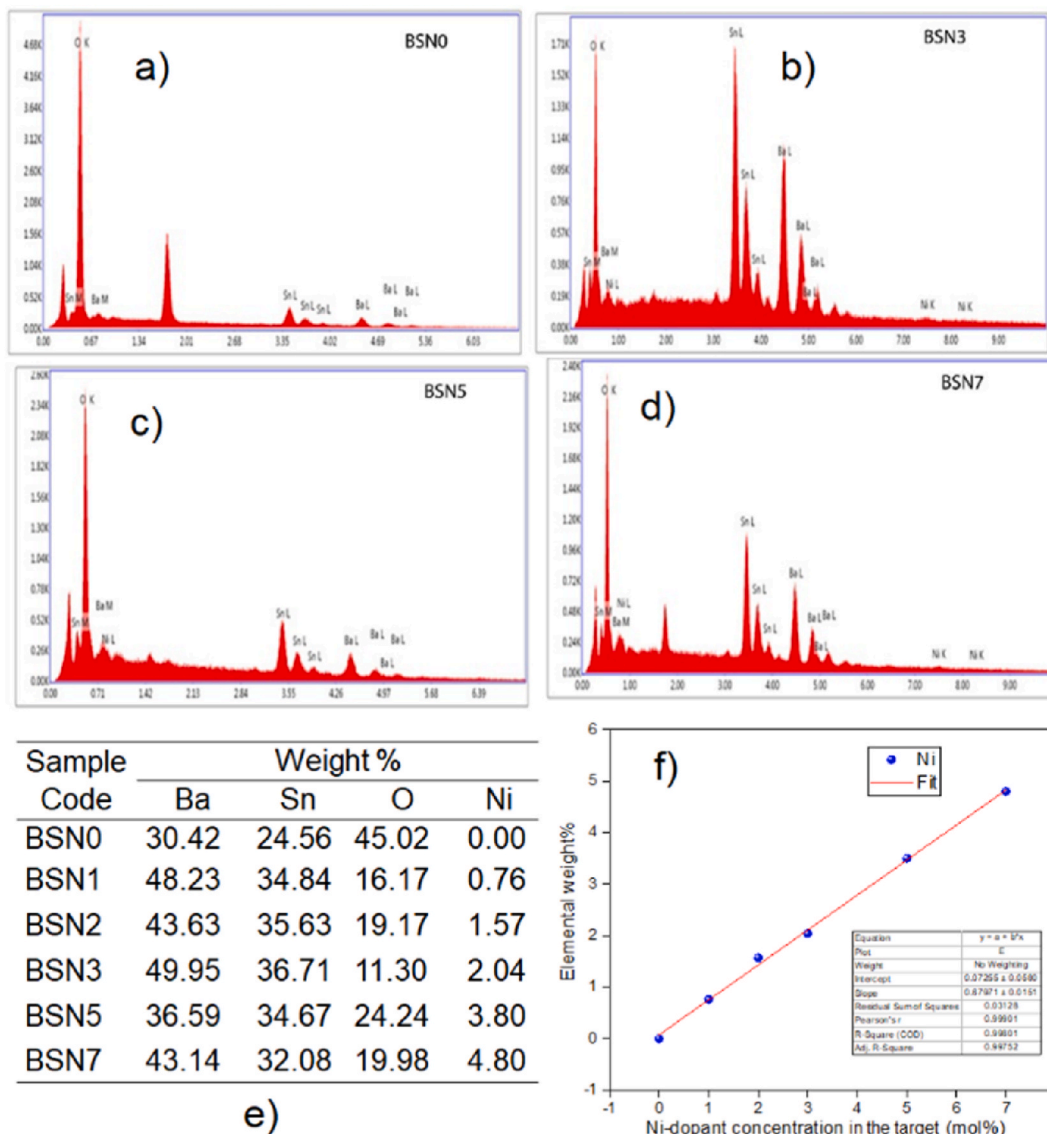


Fig. 3. (a to d) EDX spectra of selected Ni-doped BaSnO₃ films, (e) elemental composition in different films, (f) plot of Ni concentration wt% in the films vs. Ni-dopant concentration in the PLD target.

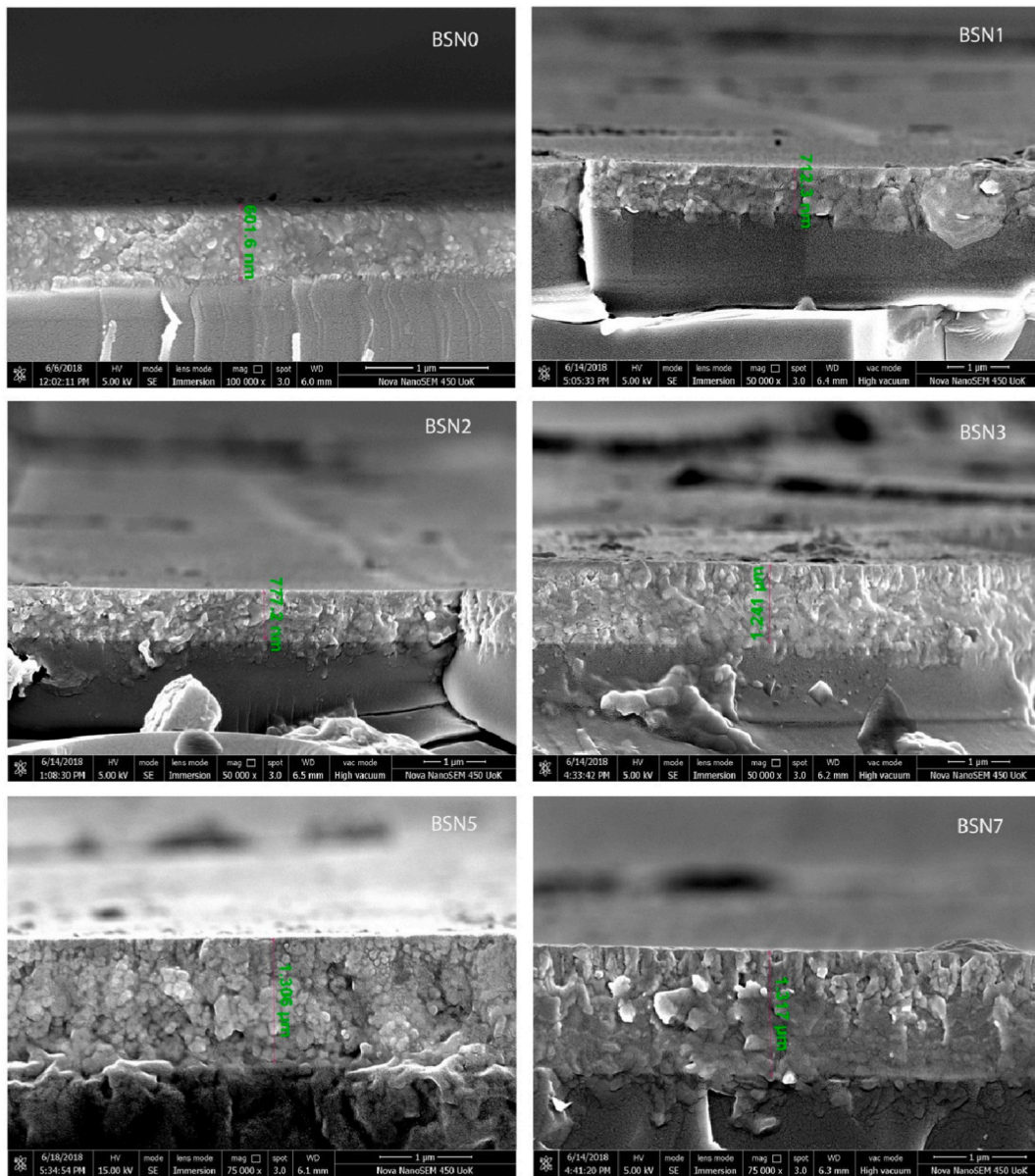


Fig. 4. Lateral FESEM images of pure and Ni:BaSnO₃ films.

of ablated material from the target occurs, and the background gas sufficiently provides the anions. In the laser ablation method, each laser pulse generated will give material sufficient for the desired phase of sub-monolayer for the deposition [31]. The film growth rate per laser pulse will depend on background gas pressure, target–substrate separation, laser energy fluence, and laser spot size [32]. In the present case, all the deposition parameters, such as background oxygen pressure, substrate nature and temperature, target–substrate separation, deposition duration, laser wavelength, spot size, and laser fluence, remain the same during deposition. To our surprise, the literature shows no report of such observation.

PLD Aurora method explains the enhancement of film deposition rate with increasing applied magnetic field [33]. It describes an enhanced ionization of the ablated particles during transport from the target to substrate through interaction between the particles and applied magnetic field by using a permanent magnet or an electromagnet in the setup. It is to be worth mentioning that, we do not apply any magnetic field externally during deposition. Hence, the observed increase in thickness cannot be attributed to Aurora PLD. Because of that, we propose a growth mechanism, the Induced Magnetic field-assisted Particle Convergence (IMPC) effect, to explain this unusual yet exciting observation.

The laser ablation generates a plasma plume at the target surface, and it may contain BaSnO_{3-x}, Ba⁺, Sn⁺, NiO_{1-x}, Ni⁺, and electrons. The adiabatic expansion of the plume rapidly removes these entities from the target surface and surges, usually outwards to the surface. The kinetic energy acquired by heavily positive ions and electrons will differ; hence, we can expect a net displacement

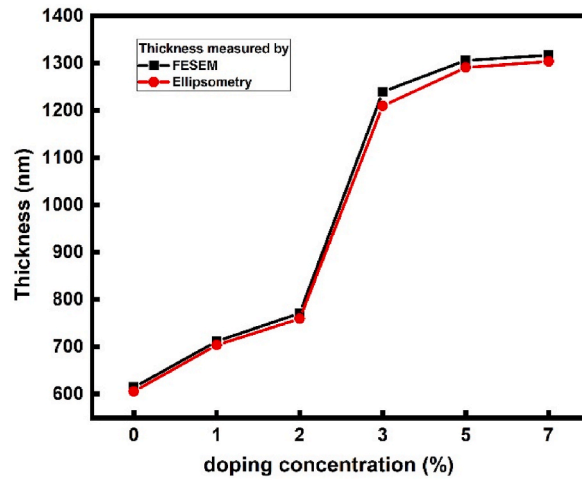


Fig. 5. The plot shows the thickness variation as a function of Ni doping concentration.

between them, leading to a net electric field pointing toward the target. The adiabatic expansion cools the temperature inside the plume, and the nickel nanoparticles may get magnetized due to the fostered electric field. Reports show that the oxygen-deficient BaSnO₃ ions are paramagnetic [12,34,35]. The induced magnetic field around the nickel can attract the otherwise diverging BaSnO_{3-x} ions (having a paramagnetic nature) toward it, leading to a convergence effect of BaSnO_{3-x} particles towards regions with higher concentrations of nickel particles within the plume. Hence, the film thickness can increase with nickel incorporation because of this

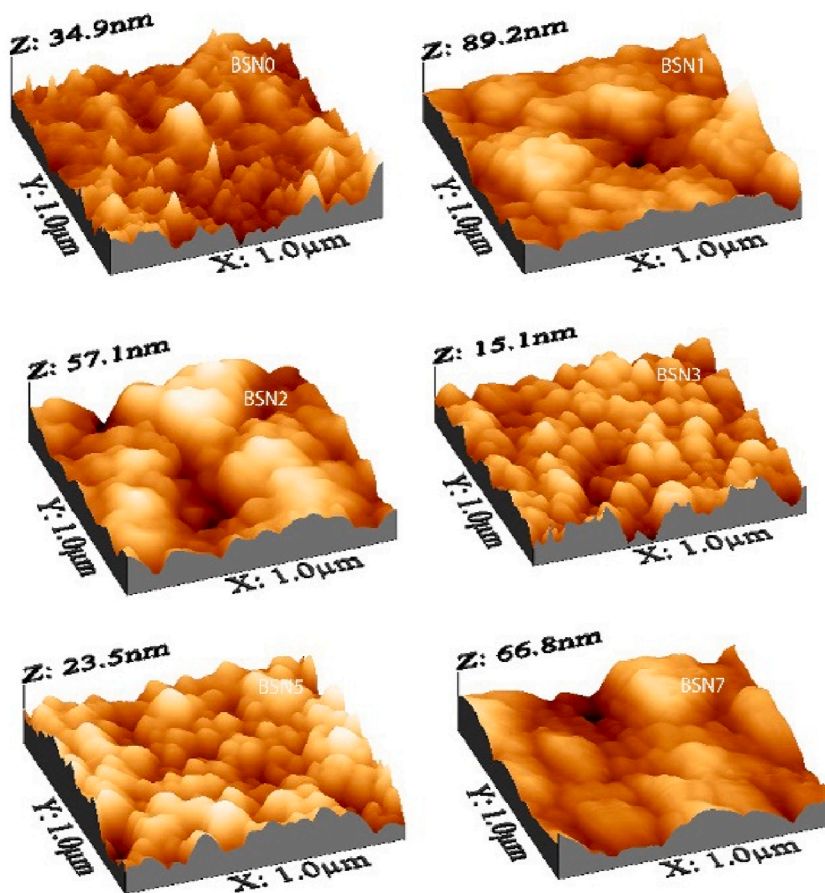


Fig. 6. AFM images of Ni-doped BaSnO₃ films.

IMPC effect in the expanding plasma plume. Espousing this assumption, due to intensified convergence of BaSnO_{3-x} ions, an increase in thickness is observed for films with enhanced Ni levels in the target material for laser ablation. With all other deposition parameters remaining intact during the deposition, except Ni concentration in the target material, we believe the presence of the IMPC effect is the most possible reason for this surprising proliferation in the film growth. We have observed a similar film thickness enhancement when BaSnO_3 films are deposited with two other dopants, which are magnetic in nature, say, Fe^{3+} and Mn^{4+} , under the same deposition conditions using PLD which is not a part of this manuscript. In this context, we wish to point out that we have so far deposited films of many materials with several non-magnetic dopants using PLD [36–39]. However, we have not observed such an unusual increase in film thickness in those cases. Hence, we strongly believe that the observed film thickness enhancement in the present can be due to the proposed IMPC effect due to the magnetic dopant ions.

AFM pictures (Fig. 6) show the surface topography and the homogeneity of BaSnO_3 films. The AFM micrograph of BSN3 shows a surface with uniform, dense isolated grains, suggesting the film's good crystalline quality. The RMS roughness estimated for the films from the AFM data is in the range of 2.33 nm–10.94 nm, indicating the smooth surface morphology of the films, suggesting their suitability for optoelectronic applications. The BSN3 film exhibits the lowest RMS roughness value of 2.33 nm (Table 1).

X-ray photoelectron spectroscopy (XPS) analyzes the surface composition and chemical states of the nickel-doped BaSnO_3 films. The survey spectrum of the BSN0 scanned from 0 to 1000 eV [Fig. S3 a], supplementary information] shows peaks corresponding to barium, tin, oxygen, and carbon. The carbon signal in the XPS spectra is due to the film surface on-air exposure contamination. The $\text{Ba}^3d_{5/2}$ and $\text{Ba}^3d_{3/2}$ doublets of the Ba^{2+} state [Fig. S3 b], supplementary information] was observed as peaks at 780.2 eV and 795.5 eV (separation = 15.3 eV) for BSN0 [40,41]. The Sn core-level spectrum [Fig. S3 c], supplementary information] displays spin-orbit doublets at 486.3 eV and 494.5 eV (separation = 8.2 eV); they can be credited to $\text{Sn}^3d_{5/2}$ and $\text{Sn}^3d_{3/2}$, indicating the Sn^{4+} state of Sn [42]. The de-convoluted O1s spectrum [Fig. S3 d], supplementary information] has three distinct peaks at 529.2, 531.2, and 532.9 eV. The peak due to lattice oxygen atoms in the perovskite structure of BaSnO_3 appears at 529.9 eV [43], and the oxygen vacancy in the BaSnO_3 film appears at 531.2 eV. The 532.9 eV peak can be due to the chemisorbed oxygen in hydroxyl form, and the observed high binding energy value stems from the formidable hydrogen bonding [44,45].

Fig. 7 displays the XPS spectrum of BSN3. The $\text{Ba}^3d_{5/2}$ and $\text{Ba}^3d_{3/2}$ doublets (Fig. 7(a)) of the Ba^{2+} state in BSN3 were observed at 780.2 eV and 795.4 eV (separation = 15.2 eV). Fig. 7(b) shows the core level spectrum of Sn with $\text{Sn}^3d_{5/2}$ and $\text{Sn}^3d_{3/2}$ doublet appears

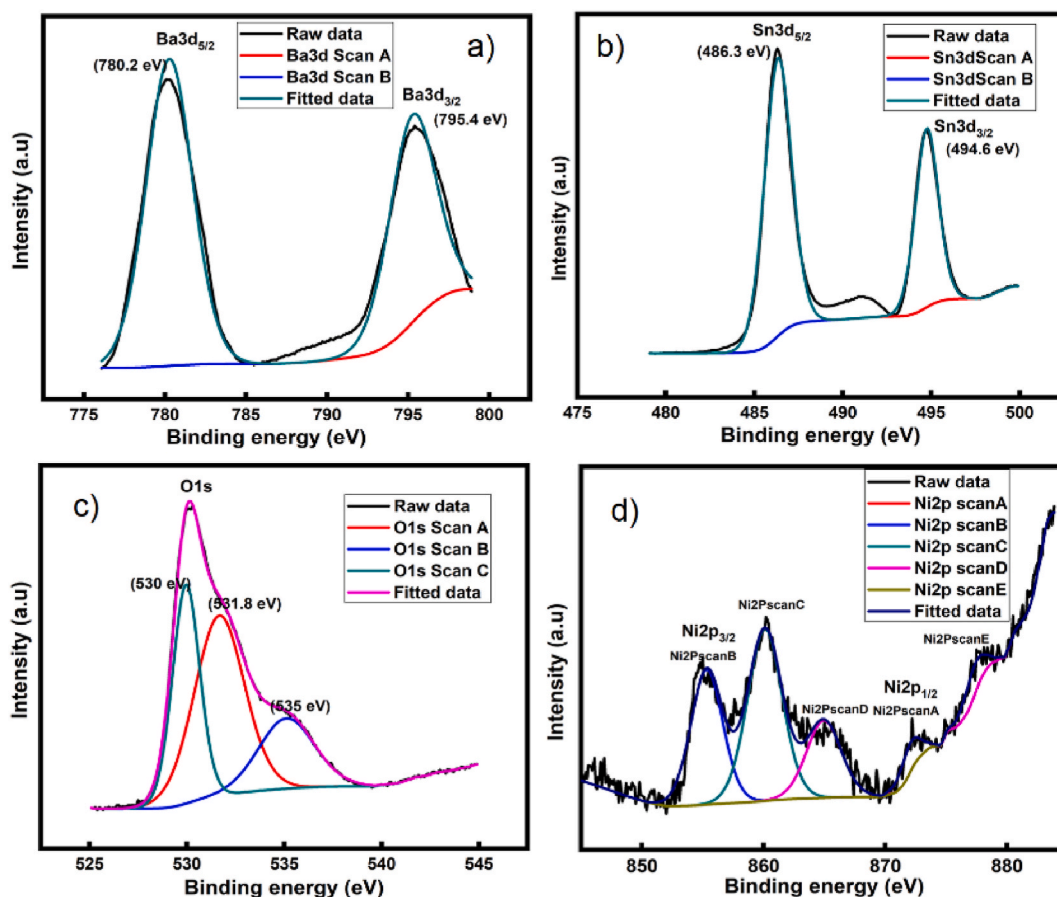


Fig. 7. XPS analysis of the laser ablated BSN3 film: (a), (b), (c), and (d) present the Core level spectra of Ba, Sn, O, and Ni respectively.

(separation = 8.3 eV) at 486.3 eV and 494.6 eV, respectively, confirming the Sn^{4+} state.

Fig. 7(c) gives the core level spectrum of oxygen in BSN3 film. The O1s peak in the BSN3 film is de-convoluted into three peaks at 530.1, 531.8, and 535 eV due to lattice oxygen atoms in the perovskite structure, oxygen vacancy in the BaSnO_3 and chemisorbed oxygen in hydroxyl form respectively. The fitted and de-convoluted Ni spectrum (Fig. 7(d)) shows two peaks at 855.4 eV and 872.8 eV due to the $\text{Ni}^2\text{p}_{3/2}$ and $\text{Ni}^2\text{p}_{1/2}$ states, respectively. The binding energy difference between these doublet peaks is 17.4 eV, corresponding to the Ni^{2+} state [46,47].

Table 2 presents the transmittance values of the films averaged over 400–2300 nm range from the transmittance data (Fig. 8). The pure film is transparent with a light grey color. However, the film's color gradually changes to dark brown with dopant level enhancement. The excellent transmittance (80–90 %) exhibited by all films indicates their good optical quality. XRD analysis also shows excellent crystalline quality for all the films. The SEM and AFM analysis suggest a smooth and uniform surface morphology for them. The observed high value of transmittance can be due to these reasons. BSN0 film shows the highest average transmittance value (90 %) among the films. From Table 2, we can see a systematic decrease in transmittance with increased Ni doping level. Surface morphology, crystallinity, thickness, strain, and defects can affect transmittance values. In the present case, we have observed that the thickness of films shows an enormous enhancement with dopant level increase. We can attribute the observed transmittance decrease in the doped films with Ni doping concentration enhancement to the enhancement in film thickness on Ni doping.

The thickness values for BSN0 and BSN7 films are 615 nm and 1317 nm, (lateral SEM data) respectively. Though there is a steep increase in film thickness with the dopant level increase, the decline in transmittance with the dopant increase is not that much. BSN7 film possesses 80% transmittance. The SEM and AFM analysis suggests a good surface feature for films. The very high crystalline quality and better surface morphology of the Ni-doped films might have reduced the effect of increased thickness on transmittance. High transparency observed for the films in the visible and infrared regions suggests their suitability for optoelectronic applications.

The bandgap energy (E_g) estimated [48,49] for the BSN0 film is 3.15 eV. The E_g value decreases regularly with increased Ni doping (Table 2). M. Khalfallah et al. observed a similar effect of bandgap narrowing in Ni-doped SnO_2 films [50]. The energy difference between the edges of the valence band (VB) and the conduction band (CB) gives the optical bandgap [51]. The O 2p orbitals constitute the top of VB, whereas the 5s orbitals of Sn form the bottom of CB [52]. The enormous dispersion among the intra-energy levels on Ni doping replaces the Sn^{4+} site in BaSnO_3 ; hence, the density of states in VB increases, creating intermittent states in the bandgap [53]. This bandgap energy renormalization with Ni doping can have various photoelectric applications.

We employ the spectroscopic ellipsometry technique for measuring the optical parameters [Fig. S4, supplementary information]. A three-layer model having the quartz substrate as the bottom layer, $\text{BaSnO}_3\text{:Ni}$ as the intermediate layer, and the $\text{BaSnO}_3\text{:Ni}$ plus voids in the top layer, and DELTAPSI2TM software was used for the optical modeling and analysis [54]. We used the Lorentz oscillator model for the analysis. We also estimated the film thickness with this technique, and the estimated values agree well with those obtained from the cross-sectional SEM analysis (Fig. 5). Cherrad et al. observed that the static index of refraction (n) of BaSnO_3 at the equilibrium constant is 2.07, which increased with photon energy [55]. We observed that n decreases systematically with wavelength, which shows normal dispersion behavior for all the films' (Fig. 9(a))

The film's extinction coefficient K also showed a behavior similar to n (Fig. 9(b)). The low value of K indicates that the optical losses due to absorption are minimal for films supporting their high transparency. The dielectric constant gives information about the reflection and loss of light when light propagates through the film [56]. The dielectric constant (both real and imaginary components ϵ_r and ϵ_i) follows a similar variation behavior with wavelength as described by n and K (Fig. 9(c and d)).

PL spectra (at excitation at 350 nm) of BaSnO_3 films show emissions extending from the near UV to the visible region with emission peaks at 385, 450, 480, and 580 nm for all the films (Fig. 10). The allowed transition from O2p to Sn5s energy levels appears at 390 nm [20]. The 450 nm emission is assigned to the charge transfer within the SnO_6 octahedra [57]. The emissions at 480 and 580 nm are due to $^3\text{P}_1^0-^1\text{D}_2$ and $^2\text{D}_{5/2}-^2\text{F}_{7/2}$ transitions of Sn [58,59]. In metal oxides, the substitution or doping of transition metal ions will cause defects due to charge compensation [60]. Both anionic and cationic vacancies are available in perovskites, and hence, this behavior can be expected [57,61]. PL peaks show no shift in position with Ni doping, but the PL intensity shows slight variations with Ni doping concentration.

Table 3 shows the electrical parameters obtained from the Hall Effect measurements. The carrier concentration obtained for BSN0 film is $2.98 \times 10^{11} \text{ cm}^{-3}$. It shows a systematic increase with Ni doping level enhancement, owing to improved crystallinity of the films. Ni doping increases the carrier mobility (Table 3), and the carrier mobility increases (by three orders) from $3.13 \text{ cm}^2\text{V}^{-1}\text{s}^{-1}$ in BSN0 to $20.93 \text{ cm}^2\text{V}^{-1}\text{s}^{-1}$ in BSN7 film. The film's electrical resistivity decreases systematically with the Ni doping level enhancement. The electrical resistivity values for BSN0 and BSN7 films are $4.05 \times 10^9 \Omega\text{cm}$ and $1.13 \times 10^3 \Omega\text{cm}$, respectively, and thus, the enhancement

Table 2
Optical parameters of Laser ablated BaSnO_3 film calculated using ellipsometry.

Sample Code	χ^2	Optical constants (at $\lambda = 550 \text{ nm}$)				Average transmittance (%)	Band gap (eV)
		(n)	(κ)	(ϵ_r)	(ϵ_i)		
BSN0	2.65	2.08	0.031	4.37	0.15	90	3.15
BSN1	1.52	2.15	0.057	4.68	0.28	88	3.12
BSN2	1.53	2.14	0.057	4.68	0.29	87	3.11
BSN3	2.65	2.05	0.112	4.72	0.46	86	3.09
BSN5	2.59	2.04	0.112	4.23	0.45	85	3.06
BSN7	2.84	2.04	0.113	4.23	0.45	80	3.01

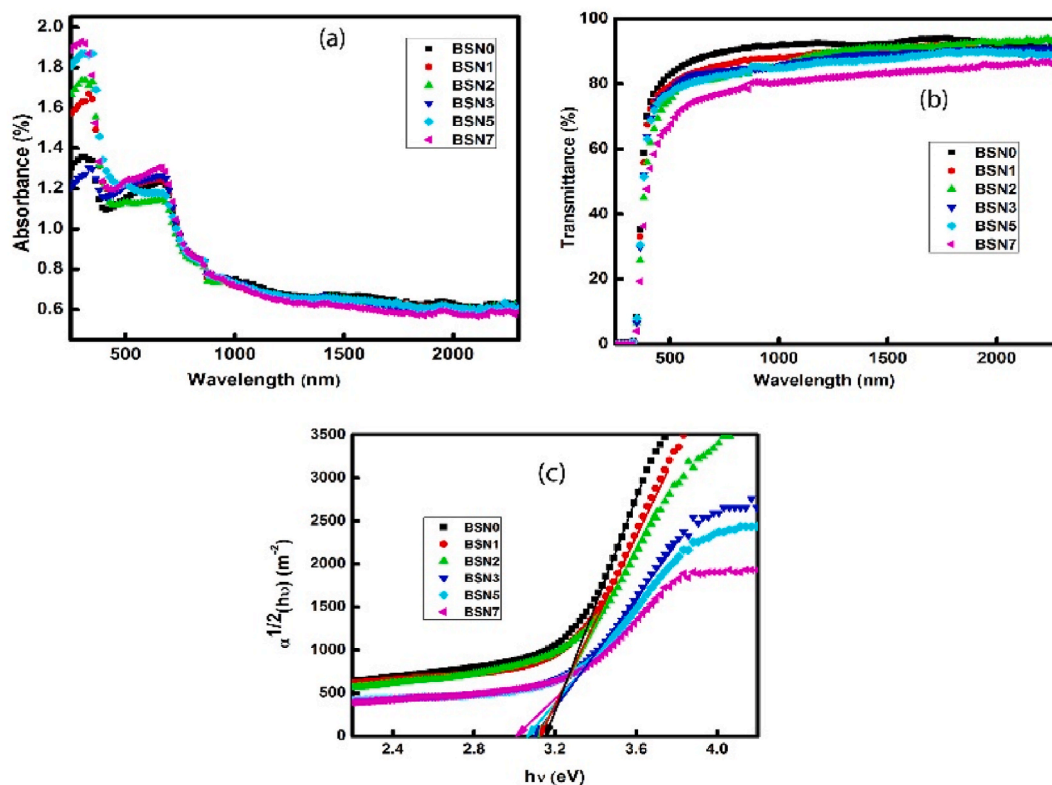


Fig. 8. a) Absorption spectra, b) transmittance spectra, and c) Tauc plot for Ni doped BaSnO₃ films.

in conductivity is of six orders with Ni-doping. This drastic and systematic increase of electrical conductivity on Ni doping can be due to the enhancement in carrier concentration, better crystallinity, and the highly ordered nature of the films.

4. Conclusion

Ni-doped BaSnO₃ films were fabricated using the PLD and analyzed their properties. XRD patterns of films reveal the polycrystalline nature with the cubic phase of BaSnO₃. Further, no additional peaks in XRD patterns imply the Ni incorporation in the BaSnO₃ lattice. The enormous increase in intensity with Ni doping suggests the improvement of crystallinity with Ni doping. The maximum XRD intensity and the least FWHM value of the most preferred orientation (110) in BSN3 film indicate its highest crystalline quality. Morphological analysis reveals the smooth surface distribution of grains of the films. The film's thickness increases enormously with the Ni doping concentration, possibly due to the Induced *Magnetic* field-assisted Particle Convergence effect. The very high transmittance of the films revealed their exemplary optical quality. The Ni doping in BaSnO₃ resulted in bandgap renormalization. XPS analysis reveals that the Ba, Sn, and Ni ions are at +2, +4, and +3 oxidation states. The refractive index, dielectric constant, and extinction coefficient show a normal dispersion behavior in all the films. The pure and doped films exhibit visible photoluminescence. Hall-effect measurement reveals the increased carrier concentration and mobility and decreased electrical resistivity with Ni doping. The high crystallinity, high transmittance, suitable surface topography, and improved electrical performances of the Ni-doped BaSnO₃ films make them excellent candidates for optical devices and solar cells.

CRedit authorship contribution statement

Jibi John: Writing – review & editing, Writing – original draft, Methodology, Investigation, Formal analysis, Data curation, Conceptualization. **S. Suresh:** Writing – review & editing, Writing – original draft, Methodology, Investigation, Formal analysis, Data curation, Conceptualization. **M. Sivakumar:** Writing – review & editing. **K.G. Gopchandran:** Writing – original draft, Supervision, Project administration, Conceptualization. **V.P. Mahadevan Pillai:** Writing – review & editing, Writing – original draft, Visualization, Validation, Supervision, Software, Resources, Project administration, Methodology, Investigation, Funding acquisition, Formal analysis, Data curation, Conceptualization.

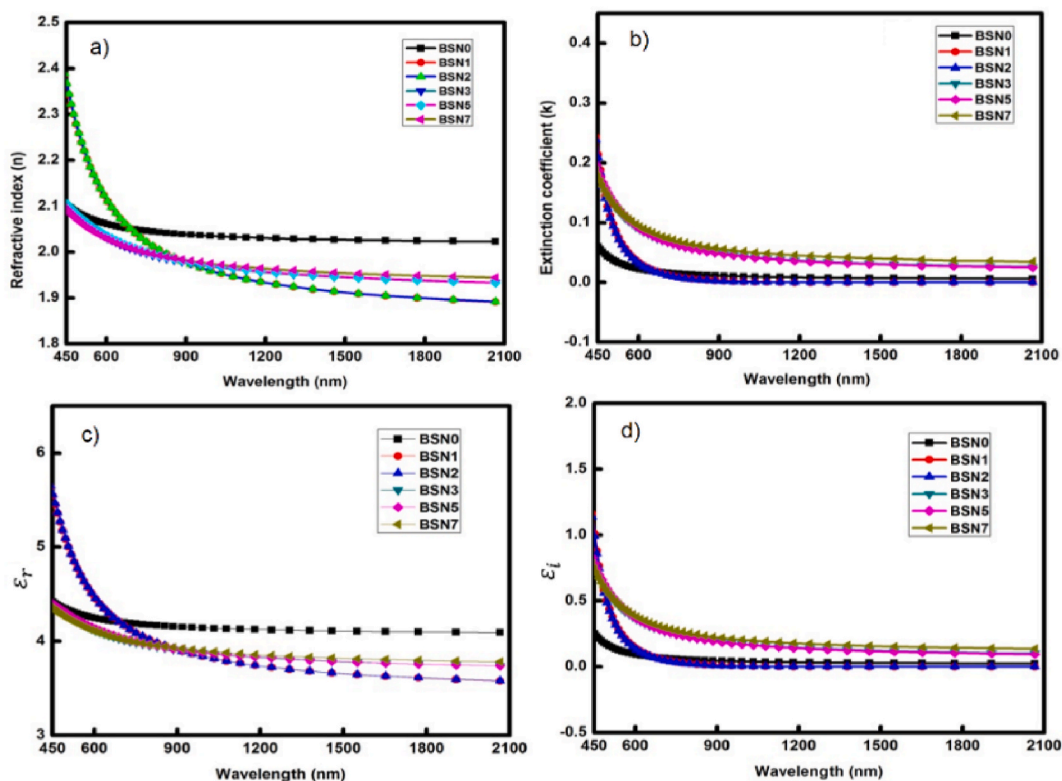


Fig. 9. Variation of optical constants with λ for Ni-doped BaSnO₃ films.

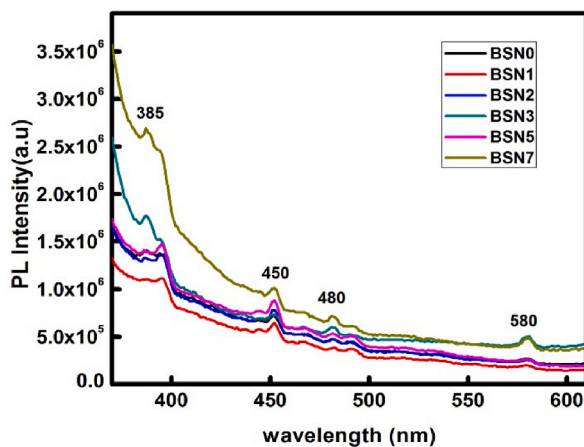


Fig. 10. PL spectra of Ni-doped BaSnO₃ films.

Table 3
Electrical parameters of BaSnO₃ films.

Sample code	Carrier concentration (cm ⁻³)	Electrical resistivity (Ω cm)	Mobility (cm ² V ⁻¹ s ⁻¹)	Carrier type
BSN0	2.98×10^{11}	4.05×10^9	3.13	n
BSN1	1.30×10^{12}	9.99×10^5	3.51	n
BSN2	4.33×10^{12}	3.47×10^5	3.66	n
BSN3	4.37×10^{12}	3.78×10^4	9.29	n
BSN5	1.78×10^{14}	1.3×10^4	15.32	n
BSN7	3.59×10^{14}	1.13×10^3	20.93	n

Declaration of competing interest

The authors declare that they have no known competing financial interests or personal relationships that could have appeared to influence the work reported in this paper.

Appendix A. Supplementary data

Supplementary data to this article can be found online at <https://doi.org/10.1016/j.heliyon.2024.e26688>.

References

- [1] H.-R. Liu, et al., *Origin of the superior conductivity of perovskite Ba(Sr)SnO₃*, Appl. Phys. Lett. 102 (11) (2013).
- [2] D. Daranciang, et al., Ultrafast photovoltaic response In Ferroelectric nanolayers, Phys. Rev. Lett. 108 (8) (2012) 087601.
- [3] U. Lampe, J. Gerblinger, H. Meixner, *Carbon-monoxide sensors based on thin films of BaSnO₃*, Sensor. Actuator. B Chem. 25 (1) (1995) 657–660.
- [4] J. Cerdà, et al., Synthesis of perovskite-type BaSnO₃ particles obtained by a new simple wet chemical route based on a sol–gel process, Mater. Lett. 56 (3) (2002) 131–136.
- [5] S. Yasuhiro, et al., Perovskite-type oxides having semiconductivity as oxygen sensors, Chem. Lett. 14 (3) (1985) 377–380.
- [6] T.R.N. Kutty, R. Vivekanadan, BaSnO₃ fine powders from hydrothermal preparations, Mater. Res. Bull. 22 (11) (1987) 1457–1465.
- [7] S. Upadhyay, O. Parkash, D. Kumar, *Preparation and characterization of barium stannate BaSnO₃*, J. Mater. Sci. Lett. 16 (16) (1997) 1330–1332.
- [8] B. Hadjarab, A. Bouguelia, M. Trari, *Optical and transport properties of lanthanum-doped stannate BaSnO₃*, J. Phys. Appl. Phys. 40 (19) (2007) 5833.
- [9] J. Cerdà, et al., Perovskite-type BaSnO₃ powders for high temperature gas sensor applications, Sensor. Actuator. B Chem. 84 (1) (2002) 21–25.
- [10] S. Upadhyay, O. Parkash, D. Kumar, Synthesis, structure and electrical behaviour of nickel-doped barium stannate, J. Alloys Compd. 432 (1) (2007) 258–264.
- [11] U. Kumar, et al., Oxygen vacancy induced electrical conduction and room temperature ferromagnetism in system BaSn_{1-x}Ni_xO₃ (0 < x < 0.20), Mater. Res. Express 4 (11) (2017) 116304.
- [12] Y. Kumar, et al., *Effect of Ni doping on structural and dielectric properties of BaTiO₃*, Indian J. Eng. Mater. Sci. 16 (2009) 390.
- [13] Y. Wang, et al., Properties of Y-doped BaSnO₃ proton conductors, Solid State Ionics 214 (2012) 45–55.
- [14] Y. Wang, et al., Influence of ZnO additive on the properties of Y-doped BaSnO₃ proton conductor, Mater. Sci. Eng., B 176 (15) (2011) 1178–1183.
- [15] Q. Liu, et al., Electrical and optical properties of Sb-doped BaSnO₃ epitaxial films grown by pulsed laser deposition, J. Phys. Appl. Phys. 43 (2010) 455401.
- [16] G. Anoop, et al., Structural, electrical, and luminescence characteristics of vacuum-annealed epitaxial (Ba,La)SnO₃ thin films, Electron. Mater. Lett. 11 (4) (2015) 565–571.
- [17] U.S. Alaan, et al., Structure and magnetism of Fe-doped BaSnO₃ thin films, AIP Adv. 7 (5) (2017).
- [18] M.Y. Shahid, et al., Synthesis, characterization and evaluation of ferroelectric and dielectric behavior of Ni-Doped Ba_{0.7}Sr_{0.3}TiO₃ thin films prepared via sol-gel route, Dig. J. Nanomater. Biostruct. 12 (2017) 1223–1231.
- [19] D.J. Singh, Q. Xu, K.P. Ong, Strain effects on the band gap and optical properties of perovskite SrSnO₃ and BaSnO₃, Appl. Phys. Lett. 104 (1) (2014).
- [20] S. Sumithra, N.V. Jaya, Tunable optical behaviour and room temperature ferromagnetism of cobalt-doped BaSnO₃ nanostructures, J. Supercond. Nov. Magnetism 31 (9) (2018) 2777–2787.
- [21] G.N. Sharma, et al., Effect of Ni substitution on the optical properties of BiFeO₃ thin films, Mater. Res. Express 3 (10) (2016) 106202.
- [22] D.-S. Gao, et al., Epitaxial Co doped BaSnO₃ thin films with tunable optical bandgap on MgO substrate, Appl. Phys. A 125 (3) (2019) 158.
- [23] T.-T. Zhang, et al., Cr-doped BaSnO₃ nanoporous thin films with tunable band gap via a facile colloidal solution route, Chem. Phys. 522 (2019) 91–98.
- [24] J. John, et al., Structural, morphological, magnetic and optical Limiting performance of Ni doped BaSnO₃, J. Electron. Mater. 50 (10) (2021) 5868–5880.
- [25] J. John, et al., Effect of manganese doping on the structural, morphological, optical, electrical, and magnetic properties of BaSnO₃, J. Mater. Sci. Mater. Electron. 31 (14) (2020) 11159–11176.
- [26] J. John, et al., Effect of Fe doping on the structural, morphological, optical, magnetic and dielectric properties of BaSnO₃, J. Mater. Sci. Mater. Electron. 32 (9) (2021) 11763–11780.
- [27] J. John, et al., Effect of substrate temperature, laser energy and post-deposition annealing on the structural, morphological and optical properties of laser-ablated perovskite BaSnO₃ films, Appl. Phys. A 125 (11) (2019) 743.
- [28] J. John, et al., Effect of oxygen pressure on the structural and optical properties of BaSnO₃ films prepared by pulsed laser deposition method, Appl. Phys. A 125 (3) (2019) 155.
- [29] A. Yildiz, et al., Ni doping effect on electrical conductivity of ZnO nanocrystalline thin films, J. Mater. Sci. Mater. Electron. 22 (9) (2011) 1473–1478.
- [30] B.D. Cullity, S.R. Stock, Elements of X-Ray Diffraction, third ed. ed, Prentice-Hall, New York, 2001.
- [31] P.R. Willmott, Quasicrystalline thin films, in: Pulsed Laser Deposition of Thin Films, 2006, pp. 633–648.
- [32] C.W. Schneider, T. Lippert, Laser ablation and thin film deposition, in: P. Schaaf (Ed.), Laser Processing of Materials: Fundamentals, Applications and Developments, Springer Berlin Heidelberg, Berlin, Heidelberg, 2010, pp. 89–112.
- [33] T. Kobayashi, H. Akiyoshi, M. Tachiki, Development of prominent PLD (Aurora method) suitable for high-quality and low-temperature film growth, Appl. Surf. Sci. 197–198 (2002) 294–303.
- [34] M. Kuppan, et al., *Structural and magnetic Properties of Ni doped SnO₂*, Adv. Condens. Matter Phys. 2014 (2014) 284237.
- [35] Y. An, et al., Oxygen vacancy-induced room temperature Ferromagnetism and Magnetoresistance in Fe-doped In₂O₃ films, J. Phys. Chem. C 119 (8) (2015) 4414–4421.
- [36] R. Vinodkumar, et al., Highly conductive and transparent laser ablated nanostructured Al: ZnO thin films, Appl. Surf. Sci. 257 (3) (2010) 708–716.
- [37] N.V. Pillai, et al., Influence of europium oxide doping on the structural and optical properties of pulsed laser ablated barium tungstate thin films, J. Alloys Compd. 509 (6) (2011) 2745–2752.
- [38] R.R. Krishnan, et al., Structural, optical, and morphological properties of laser ablated ZnO doped Ta₂O₅ films, Mater. Sci. Eng., B 174 (1) (2010) 150–158.
- [39] J.R. Rani, et al., *Structural and nonlinear optical properties of self-assembled SnO₂-doped silicon nanorings Formed by pulsed laser ablation*, Electrochem. Solid State Lett. 11 (8) (2008) K73.
- [40] M.R. Manju, et al., Enhancement of ferromagnetic properties in composites of BaSnO₃ and CoFe₂O₄, J. Magn. Magn Mater. 452 (2018) 23–29.
- [41] P. Singh, et al., Electronic structure, Electrical and dielectric Properties of BaSnO₃ below 300 K, Jpn. J. Appl. Phys. 47 (5R) (2008) 3540.
- [42] M. Kwoka, et al., XPS study of the surface chemistry of L-CVD SnO₂ thin films after oxidation, Thin Solid Films 490 (1) (2005) 36–42.
- [43] Z. Saroukhani, et al., Effect of working pressure and annealing temperature on microstructure and surface chemical composition of barium strontium titanate films grown by pulsed laser deposition, Bull. Mater. Sci. 38 (6) (2015) 1645–1650.
- [44] P. Prieto, et al., XPS study of silver, nickel and bimetallic silver–nickel nanoparticles prepared by seed-mediated growth, Appl. Surf. Sci. 258 (22) (2012) 8807–8813.
- [45] S. Jaiswar, K.D. Mandal, Evidence of enhanced oxygen vacancy defects inducing ferromagnetism in multiferroic CaMn₇O₁₂ Manganite with sintering time, J. Phys. Chem. C 121 (36) (2017) 19586–19601.

- [46] K.H. Wong, et al., Enhanced photocurrent and stability of organic solar cells using solution-based NiO interfacial layer, *Sol. Energy* 86 (11) (2012) 3190–3195.
- [47] H.-q. Wang, et al., In situ growth of NiO nanoparticles on carbon paper as a cathode for rechargeable Li–O₂ batteries, *RSC Adv.* 7 (38) (2017) 23328–23333.
- [48] D. Beena, et al., Effect of substrate temperature on structural, optical and electrical properties of pulsed laser ablated nanostructured indium oxide films, *Appl. Surf. Sci.* 255 (20) (2009) 8334–8342.
- [49] J. Tauc, Optical properties of Amorphous semiconductors, in: J. Tauc (Ed.), *Amorphous and Liquid Semiconductors*, Springer US, Boston, MA, 1974, pp. 159–220.
- [50] M. Khalfallah, et al., Hydrophilic nickel doped porous SnO₂ thin films prepared by spray pyrolysis, *Phys. Scripta* 95 (9) (2020) 095805.
- [51] S. Nandy, et al., Enhanced p-type conductivity and band gap narrowing in heavily Al doped NiO thin films deposited by RF magnetron sputtering, *J. Phys. Condens. Matter* 21 (11) (2009) 115804.
- [52] T. Schumann, et al., Structure and optical band gaps of (Ba,Sr)SnO₃ films grown by molecular beam epitaxy, *J. Vac. Sci. Technol. A* 34 (5) (2016).
- [53] H. Mizoguchi, et al., A germanate transparent conductive oxide, *Nat. Commun.* 2 (1) (2011) 470.
- [54] Introduction to spectroscopic ellipsometry, in: *Spectroscopic Ellipsometry*, 2007, pp. 1–11.
- [55] D. Cherrad, et al., Influence of valence electron concentration on elastic, electronic and optical properties of the alkaline-earth tin oxides A₃SnO (A=Ca, Sr and Ba): a comparative study with ASnO₃ compounds, *Phys. B Condens. Matter* 406 (14) (2011) 2714–2722.
- [56] C.V. Ramana, et al., Growth and surface characterization of sputter-deposited molybdenum oxide thin films, *Appl. Surf. Sci.* 253 (12) (2007) 5368–5374.
- [57] N. Rajamanickam, K. Jayakumar, K. Ramachandran, Effect of iron doping on magnetic and electrical properties of BaSnO₃ nanostructures, *J. Mater. Sci. Mater. Electron.* 29 (23) (2018) 19880–19888.
- [58] H. Feng, Y. Yang, X. Wang, Microwave radiation heating synthesis and luminescence of SrWO₄ and SrWO₄:xEu³⁺ powders, *Ceram. Int.* 40 (7) (2014) 10115–10118. Part A).
- [59] A.S. Deepa, et al., Structural and optical characterization of BaSnO₃ nanopowder synthesized through a novel combustion technique, *J. Alloys Compd.* 509 (5) (2011) 1830–1835.
- [60] P. Doidge, in: R. Payling, P.L. Larkins (Eds.), *Optical Emission Lines of the Elements*, John Wiley and Sons, 2000, pp. 381–383. *Book (688 pages) and companion CD-ROM.* Publisher's prices: 1350DM; €690.24; US\$750; £395. *Spectrochimica Acta Part B: Atomic Spectroscopy*, 2002. 57.
- [61] G. Sanal Kumar, et al., Terbium oxide doped MoO₃ nanostructures: Morphology engineering and enhanced photoluminescence, *J. Alloys Compd.* 698 (2017) 215–227.